

Electronic and vibrational properties of V₂C-based MXenes: From experiments to first-principles modeling

Aurélie Champagne,^{1,*} Lu Shi,^{1,2} Thierry Ouisse,² Benoît Hackens,¹ and Jean-Christophe Charlier^{1,†}

¹*Institute of Condensed Matter and Nanoscience, Université catholique de Louvain, B-1348 Louvain-la-Neuve, Belgium*

²*Laboratoire des Matériaux et du Génie Physique, Université Grenoble Alpes, 38000 Grenoble, France*



(Received 3 October 2017; revised manuscript received 12 March 2018; published 26 March 2018)

In the present work, the electronic and vibrational properties of both pristine V₂C and fully terminated V₂CT₂ (where T = F, O, OH) two-dimensional monolayers are investigated using density functional theory. First, the atomic structures of V₂C-based MXene phases are optimized, and their respective dynamical stabilities are discussed. Second, electronic band structures are computed indicating that V₂C is metallic as well as all the corresponding functionalized systems. Third, the vibrational properties (phonon frequencies and spectra) of V₂C-based MXenes are computed with the density functional perturbation theory and reported. Both Raman-active (E_g , A_{1g}) and infrared-active (E_u , A_{2u}) vibrational modes are predicted *ab initio* with the aim to correlate the experimental Raman peaks with the calculated vibrational modes and to assign them to specific atomic motions.

The effect of the terminal groups on the vibrational properties is emphasized, along with the effect on the presence and position of the corresponding Raman peaks. Our results provide insights for the identification and characterization of V₂C-based samples using Raman spectroscopy.

DOI: [10.1103/PhysRevB.97.115439](https://doi.org/10.1103/PhysRevB.97.115439)

I. INTRODUCTION

Since the discovery of graphene and its outstanding properties [1,2], two-dimensional (2D) materials have attracted much interest in the field of material science and device processing. Purely 2D crystals are a subclass of nanomaterials that exhibit interesting physical characteristics due to the quantum confinement of their electrons. At present, more than a dozen different 2D crystals have been reported [3], including hexagonal boron nitride [4], transition-metal dichalcogenides (MoS₂, MoSe₂, WS₂, NbSe₂, . . .) [5], thin oxide layers (TiO₂, MoO₃, WO₃, . . .), silicene [6], phosphorene [7], germanene [8,9], stanene, borophene, etc. These novel 2D systems also exhibit exotic properties suggesting new possible applications. However, the lack of flexibility in their chemical composition and the weak interlayer (van der Waals) interactions limit their use. Recently, the family of 2D materials has been significantly expanded by introducing 2D layers of transition-metal carbides, nitrides, and carbonitrides, known as MXenes [10–13]. MXenes have been shown to be very promising building blocks of an impressive number of potential applications, including energy storage devices [14], such as hydrogen storage [15], Li and multivalent ion batteries [16–20], and electrochemical capacitors [21–26], thermoelectric materials [27], sensors [28], and actuators [29,30]. Another exciting physical property is their extreme volumetric capacitance, exceeding 900 F cm⁻³, while the best one reported for a carbon-based electrode is around 300 F cm⁻³ [19,20]. Moreover, they exhibit good electromagnetic interference shielding abilities [31]. First-principles calculations indicate good mechanical properties, including high elastic constant [32] and flexibility [33]. Finally,

they can potentially pave the way for future spintronics devices since their electronic and magnetic properties can be tuned via surface functionalization [34,35].

MXene structures are generally produced by selectively etching layers of *sp* elements from their corresponding three-dimensional (3D) MAX phase. The MAX phases are layered 3D solids composed of 2D sheets of *MX* separated by *A* layers [36], thus exhibiting a general formula $M_{n+1}AX_n$, where *M* represents an early transition metal (Sc, Ti, V, Cr, Zr, Nb, Mo, Hf, Ta), *A* represents an element from groups 13 to 16 (Al, Si, P, Ga, Ge, As, In, Sn), *X* represents either a carbon or a nitrogen atom, and *n* varies from 1 to 3. In contrast to graphitelike materials with strong intralayer covalent bonds and weak van der Waals interlayer interactions, the MAX phases are mostly composed of covalent, ionic, and metallic strong bonds. The chemical bonds between *A* and $M_{n+1}X_n$ are weaker than those between *M* and *X*, allowing for the extraction of *A* layers from the 3D crystals [10]. Although the removal of *A* layers from the MAX phases cannot be achieved with the usual mechanical exfoliation method [10], Barsoum and coworkers demonstrated the removal of Al layers from the Ti₃AlC₂ MAX phase by hydrofluoric acid treatment and sonication [10], resulting in a 3D to 2D transformation. Today, more than 20 separate MXenes have been successfully synthesized using a similar procedure, and dozens more have been predicted [11]. However, it is still presently highly challenging to exfoliate pure MXene monosheets from the 3D MAX phase. In addition, due to the use of etching agents, MXenes are always terminated with functional surface groups, such as –F, =O, and –OH, that are randomly distributed [12]. This random distribution of the terminal groups was confirmed by electron-energy-loss spectroscopy in transmission electron microscopy [37], nuclear magnetic resonance spectroscopy [22,38], and x-ray photoelectron spectroscopy [39] for various transition-metal carbides. The general formula of these chemically terminated

*aurelie.champagne@uclouvain.be

†jean-christophe.charlier@uclouvain.be

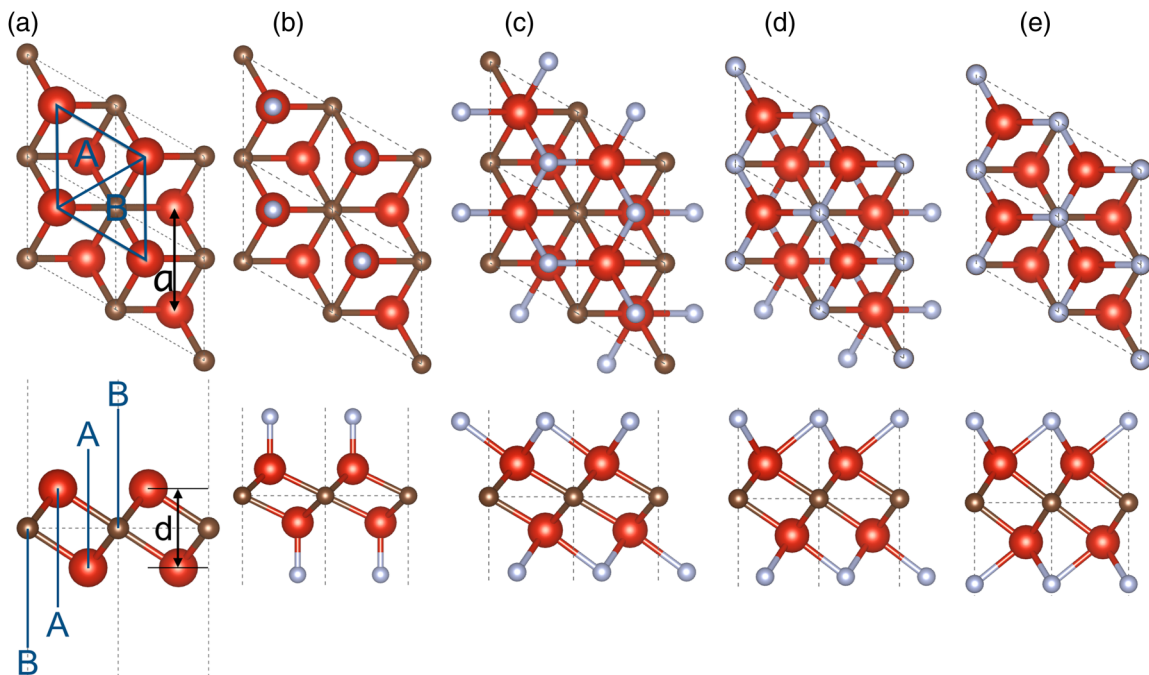


FIG. 1. Atomic structure of (a) pristine V_2C and four models for terminated V_2CT_2 : (b) MD1, (c) MD2, (d) MD3, and (e) MD4, top and side views. Vanadium and carbon atoms are in red (medium gray) and brown (dark gray), respectively, while the functional group ($T = F, O, OH$) is in blue (light gray). In (a), A and B indicate the two types of hollow sites; a and d are the lattice constant and the layer thickness, respectively.

MXene crystals is therefore $M_{n+1}X_nT_{n+1}$ where T represents the terminal groups [12].

In the present work, the structural and electronic properties of V_2C -based MXenes (pristine and V_2CT_2 systems terminated with $T = F, O$ and OH) are investigated using first-principles density functional theory techniques [40,41]. When considering a nonzero magnetic moment for the V atoms, Hu *et al.* [20] found that the antiferromagnetic configuration is the most stable phase for V_2C , with a very small magnetic moment around $0.14\mu_B$ [34,42]. Given that there is no experimental evidence of magnetic properties for the V_2C system as confirmed by the present *ab initio* simulations, only the nonmagnetic phases of V_2C systems will be considered here. The dynamical stability is studied for different functionalization configurations based on the density functional perturbation theory approach [43,44]. Atomic structures exhibiting imaginary vibrational frequencies are noted as dynamically unstable. Both Raman-active (E_g and A_{1g}) and infrared-active (E_u and A_{2u}) vibrational modes, which are presently missing in the literature, are predicted *ab initio*. Electronic properties, including electronic band structures and densities of states (DOSs), and vibrational properties such as Raman spectra are reported and directly compared to experimental measurements. A similar investigation was recently done for Ti_3C_2 -based systems [45], while a stability study based on phonon frequency investigation was done for various single-layer MXene structures [14].

II. COMPUTATIONAL DETAILS AND CHARACTERIZATION TECHNIQUES

The structural, electronic, and vibrational properties are calculated with the ABINIT package [46,47], which is based

on plane-wave basis sets to represent the electronic wave functions and charge density. *Ab initio* calculations are performed using the generalized gradient approximation (GGA) for the exchange-correlation functional, as proposed by Perdew, Burke, and Ernzerhof (PBE) [48]. As the partially filled d bands and thus localized electrons in V atoms are usually not well represented by the GGA functional, the GGA plus Hubbard U (GGA+ U) [49,50] functional is used to predict the electronic properties with a Hubbard correction of ~ 4 eV for the V atoms, as also considered in previous works [20,51]. Optimized norm-conserving Vanderbilt pseudopotentials (ONCVSP-PBE) [52] are used to describe the core-valence interaction. Configurations of H $1s^1$, C $2s^22p^2$, O $2s^22p^4$, F $2s^22p^5$, and V $3s^23p^63d^34s^2$ are treated as valence electrons. A plane-wave basis set with a converged energy cutoff of 80 Ry is used to represent the wave functions. The first Brillouin zone is sampled with an $18 \times 18 \times 1$ Monkhorst-Pack k -point grid. The atomic positions are optimized until the largest force is smaller than $2.5 \cdot 10^{-4}$ eV/Å. To prevent an undesired interaction between isolated monolayers, a vacuum spacing of at least 10 Å is introduced. Spin-orbit coupling (SOC) effects have shown a negligible influence on our computed structural and electronic properties of V_2C -based MXene. Hence, the following results are presented without taking SOC effects into account.

In order to validate the calculations, Raman measurements of exfoliated flakes are also carried out. We start sample preparation from V_2AlC single crystals prepared using a method reported previously [53]. The flakes are synthesized by etching Al layers from V_2AlC by immersing the 3D crystal in diluted (40 wt %) hydrofluoric acid (HF) for 72 h at room temperature. Sonication is then performed in the 40 wt % HF

TABLE I. Structural parameters and formation energies for pristine V_2C and MD1–MD4 functionalized systems. The ground-state (GS) configuration of V_2CO_2 is also included.

	Model	Lattice parameter a (Å)	V-V distance (Å)	Thickness d (Å)	Formation energy (eV)
V_2C		2.89	2.18	2.18	0
V_2CF_2	MD1	3.20	1.79	5.28	−8.65
	MD2	2.99	2.04	4.59	−9.45
	MD3	2.89	2.24	4.90	−8.94
	MD4	2.80	2.49	5.12	−9.10
V_2CO_2	MD1	3.13	2.14	5.31	−7.35
	MD2	2.90	2.38	4.40	−9.40
	MD3	2.86	2.41	4.54	−9.13
	MD4	2.82	2.48	4.70	−8.78
	GS	2.89	2.38	4.40	−9.40
$V_2C(OH)_2$	MD1	3.22	1.78	7.24	−7.98
	MD2	3.00	2.06	6.54	−9.41
	MD3	2.93	2.24	6.77	−9.02
	MD4	2.85	2.45	6.94	−9.16
$V_2CF(OH)$	MD1	3.21	1.79	6.26	−8.39
	MD2	2.99	2.05	5.58	−9.46
	MD3	2.91	2.24	5.86	−8.96
	MD4	2.83	2.47	6.04	−9.14

solution at 80 °C for 8 h, with the aim to separate the layered solid into flakes. The exfoliated flakes are then washed with deionized water and dried. The presence of terminal groups is evidenced by energy dispersive spectroscopy (EDS) measurements, reporting an atomic ratio of 28:35:27:10 for V:C:O:F, respectively [54], which is purely qualitative since quantitative measurements are not easily performed on light elements. For micro-Raman measurements, the V_2C -based MXene flakes are simply deposited on a glass slide and not transferred on a substrate. Raman spectroscopy is performed at room temperature with a LabRam Horiba spectrometer with a laser wavelength of 514 nm. The laser beam is focused on the sample with a 100× objective (numerical aperture of 0.95), and the incident power is kept below 1 mW. A grating of 2400 lines/mm is used in order to achieve a high spectral resolution.

III. RESULTS AND DISCUSSION

A. Structural properties

The ground-state structure of the pristine V_2C with fully relaxed geometry is found to be hexagonal. The unit cell includes three atoms, two vanadium and one carbon, which resides in the $P\bar{3}m1$ space group. The V atoms are located at $(\frac{1}{3}, \frac{2}{3}, z)$ and $(\frac{2}{3}, \frac{1}{3}, -z)$ on the $2d$ Wyckoff sites, and the C atom is located at $(0,0,0)$ on the $1a$ Wyckoff site. These atoms are therefore arranged in a triple-layer structure where the C layer is sandwiched between the two V layers, as illustrated in Fig. 1(a). The lattice constant a is equal to 2.89 Å, and the layer thickness d , defined as the V-V distance, equals 2.18 Å [Fig. 1(a)].

Based on the unit cell of pristine V_2C , functionalized V_2CT_2 MXene structures with $T = F, O,$ and OH terminations are constructed. Two types of hollow sites on the surface of V_2C can be distinguished: A sites correspond to fcc sites for which no C atom is present under the V atoms, while B

sites correspond to hcp sites located on the top of a C atom [Fig. 1(a)]. As previously proposed by Khazaei *et al.* [28], different functionalization models can be built according to the lattice positions of the termination groups. Four models are proposed here [Figs. 1(b)–1(e)]. In model 1 (MD1), two functional groups of the same type (F, O, or OH) are positioned on the top of the two transition-metal atoms V [Fig. 1(b)]. In the case of model 2 (MD2), the two functional groups are located on the top of the hollow sites A [Fig. 1(c)]. Model 3 (MD3) considers one functional group on the top of hollow site A and a second functional group of the same type on the top of hollow site B [Fig. 1(d)]. Last, model 4 (MD4) presents two functional groups located on the top of hollow sites B [Fig. 1(e)]. For each type of functionalization, the four configurations are systematically investigated, and their respective stability are compared. The relative structural stabilities of the four models usually depend on the possibility for the transition metal to provide sufficient electrons to both the carbon atoms and the functional groups [28]. Table I summarizes the structural parameters computed *ab initio* for the four models. To ascertain the stability of the functionalized V_2CT_2 MXene monosheets and in order to determine the most stable configuration for each system, the formation energies are computed according to the following formula [55]:

$$\Delta H_f = E_{\text{tot}}(V_2CT_2) - E_{\text{tot}}(V_2C) - E_{\text{tot}}(T_2) - 2\mu_T, \quad (1)$$

where $E_{\text{tot}}(V_2C)$ and $E_{\text{tot}}(V_2CT_2)$ stand for the total energy of the pristine and terminated MXene, respectively. Depending on the terminal groups, $E_{\text{tot}}(T_2)$ corresponds to the total energy of F_2 , O_2 , or $O_2 + H_2$, and μ_T is the chemical potential of the chemisorbed groups. For all the terminated structures, the MXene surfaces are assumed to be fully terminated with no pending bond remaining, as suggested by Khazaei *et al.* [28], and μ_T is fixed at 0.0 eV. The large negative values reported in Table I, corresponding to the formation energies of all V_2CT_2 systems, indicate the spontaneous and exothermic formation

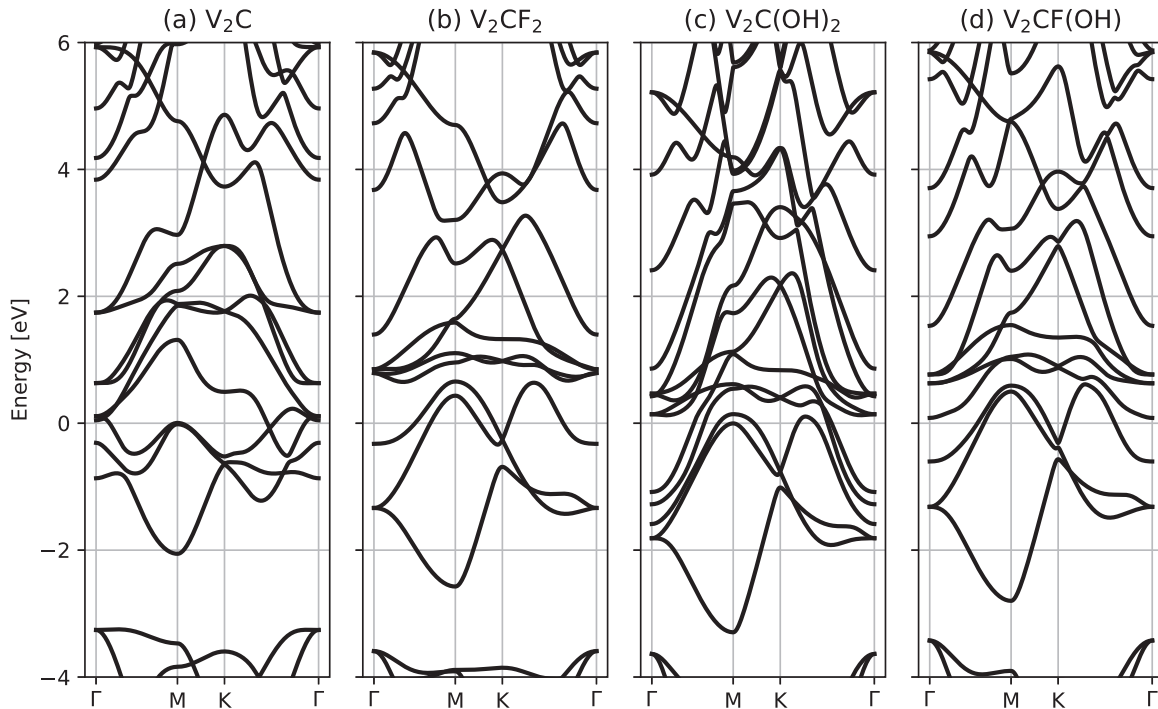


FIG. 2. Electronic band structures of (a) V_2C , (b) V_2CF_2 , (c) $V_2C(OH)_2$, and (d) $V_2CF(OH)$ in their high-symmetry configuration. The Fermi level is fixed as the reference of zero energy.

of strong ionic bonds between vanadium atoms and terminal groups [28]. In addition, it is found that the energetically favored structures for V_2C -based systems functionalized with F, O, and OH correspond to MD2, where the terminal groups occupy fcc sites. However, MD2 is dynamically unstable for V_2CO_2 as the corresponding phonon band structure presents imaginary vibrational frequencies. Therefore, among the four models, MD3 is assigned to the stable configuration for V_2CO_2 . Neither MD1 nor MD4 is a good candidate for V_2CT_2 systems. While the ground-state structures for V_2CF_2 and $V_2C(OH)_2$ systems correspond to the MD2 configurations, a low-symmetry configuration (space group $P1$) is found for V_2CO_2 as the ground-state structure which is close to the symmetric MD2, although with a slight modification of the atomic coordinates of both V and C atoms. This different behavior between an O-terminated system and the F- and OH-terminated ones might come from the additional unpaired electron in oxygen with respect to fluorine and hydroxide groups. As symmetries in crystal structures allow an easier interpretation of both electronic and vibrational properties, the following sections deal with only pristine V_2C and functionalized V_2CF_2 and $V_2C(OH)_2$ systems.

B. Electronic properties

According to its electronic band structure, the V_2C monosheet exhibits a metallic behavior. In contrast to the well-studied Ti_3C_2 MXene system which undergoes a metallic to indirect band gap semiconductor transition [45], V_2CT_2 structures preserve their metallic character. Figures 2(a)–2(c) show the calculated band structures of V_2C , V_2CF_2 , and $V_2C(OH)_2$, respectively, which are in agreement with previous calculations [27,42,56]. A band gap opening was observed by Hu *et al.*

[20] only for the terminated V_2CT_2 in the antiferromagnetic configuration. At first sight, these band structures show some similarities, and as both the $-F$ and $-OH$ groups are able to catch only one electron from the pristine surfaces, they seem to affect the electronic band structure of V_2C in a similar way. However, a precise analysis of the number and origin of the bands crossing the Fermi level could provide more information regarding the electronic properties and highlight the role played by the terminal groups.

Therefore, for both V_2C and V_2CT_2 ($T = F, OH$) systems, the local density of states (LDOS) for each atom is computed and shown in Fig. 3. Moreover, in order to investigate the contribution of each atomic orbital in the LDOS, the projected densities of states (PDOSs) are also calculated.

When bringing atoms in close proximity, strong chemical bonds such as ionic and covalent bonds are formed, respectively, from the transfer and sharing of electrons between atoms. The two electrons involved in bonding are coupled together with a bond strength depending on the overlap between their atomic energy levels. Metal atoms usually take part in bonding via their partially filled valence orbitals. Therefore, in V_2C -based systems, the C atom is involved in the bonding states through its outmost $2s$ and $2p$ orbitals, and V atoms are mainly involved through their $3d$ orbitals. In Fig. 3(a), both LDOS and PDOS of pristine V_2C are presented, and information on the hybridization of V $3d$, C $2p$, and C $2s$ orbitals can be used to discuss the nature of the bonding states. In the lowest-energy region, the states around 11 and 13 eV below the Fermi level can be regarded as bonding states between the C $2s$ and V $3d$ orbitals. The PDOSs of C $2p$ orbitals are mainly distributed between -6 and -3 eV. These states can clearly be assigned to bonding states between the C $2p$ and the V $3d$ orbitals. Around -3 eV, there is a

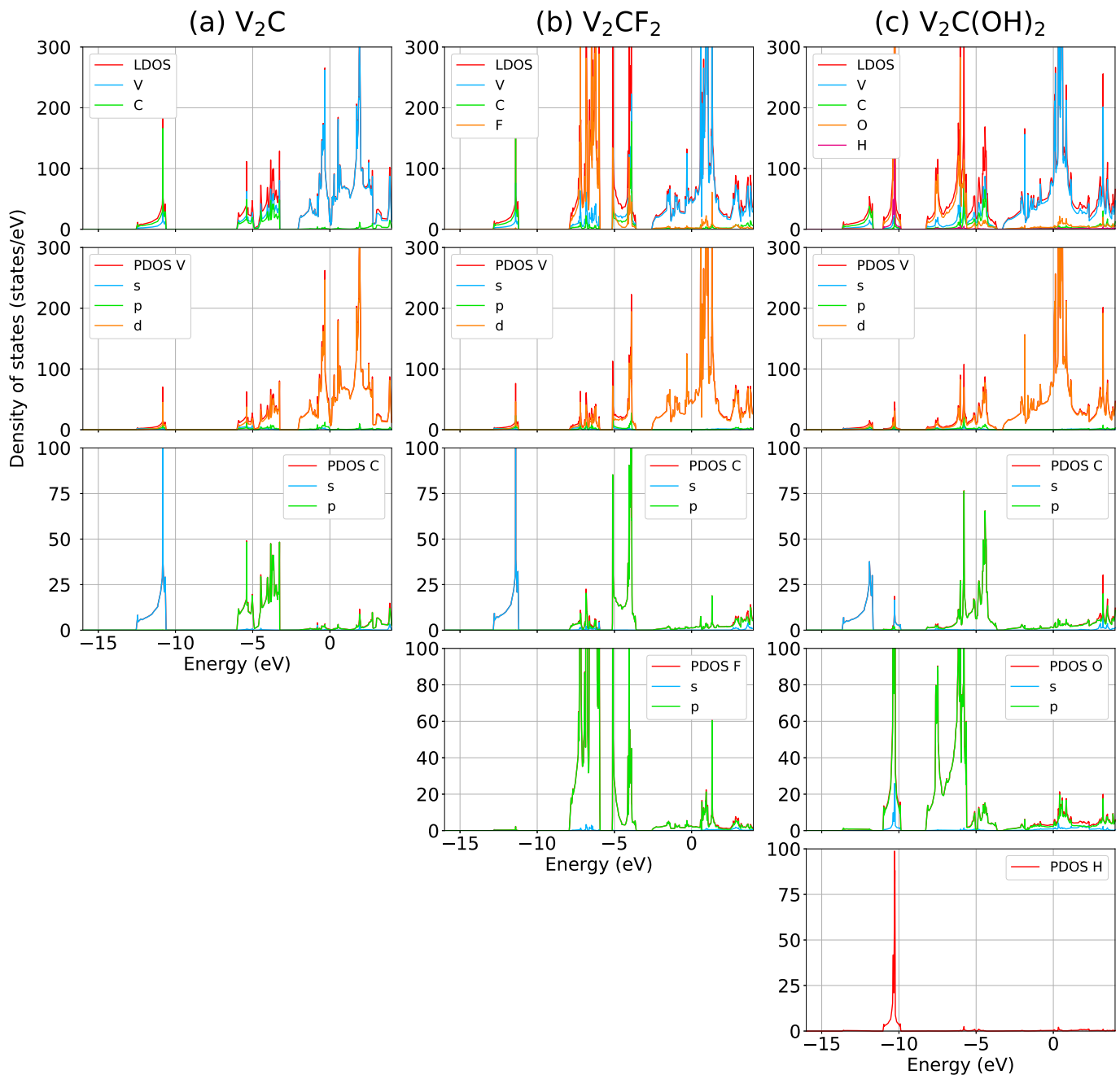


FIG. 3. Local and projected densities of states of (a) V_2C , (b) V_2CF_2 , and (c) $V_2C(OH)_2$ in their high-symmetry configuration. The Fermi level is positioned at zero energy.

pseudogap of about 1 eV which can be seen as the separation between the bonding and antibonding states. Finally, the states in the vicinity of the Fermi level (from -2 eV and above) correspond to V $3d$ states and are expected to give rise to electrical conductivity in the V_2C system [Fig. 3(a)]. Upon functionalization, the atomic orbitals from the terminal groups add up in the LDOS and PDOS features. In the PDOS of V_2CF_2 , the F $2p$ orbitals are mainly located between -8 and -4 eV and can be attributed to bonding states between V $3d$ and F $2p$ orbitals [Fig. 3(b)]. Some F $2p$ states are also found near the Fermi energy and ensure the metallic character of V_2CF_2 . In the PDOS of $V_2C(OH)_2$, the O $2p$ orbitals are mainly distributed between -8 and -4 eV and

can be assigned to bonding states between V $3d$ and O $2p$ orbitals [Fig. 3(c)]. Moreover, due to the presence of hydrogen atoms, some bonding states between O $2p$ and H $1s$ orbitals are found in the energy range between -11 and -10 eV. In comparison with V_2CF_2 , some O $2p$ orbitals are also found around the Fermi level. The general bonding character of both V_2C and V_2CF_2 systems may be described as covalent ionic and metallic. The former can be explained by the hybridization of the V $3d$ states with the C $2p$ and F $2p$ /O $2p$ states presenting an important electronegativity difference, while the latter is due to the resonance of the $3d$ orbitals of the vanadium atoms around the Fermi level [57]. Finally, upon adsorption of F or OH groups onto the V_2C surfaces, each F or OH group obtains

one electron from V_2C , leading to a slight shift of the Fermi level and of the V $3d$, C $2s$, and C $2p$ bands [Figs. 3(b) and 3(c)]. This shift is not significant and indicates that the V-C bonds in the different V_2C -based systems are relatively similar, explaining also the very similar V-V distances of ~ 2.0 – 2.2 Å (Table I).

Our theoretical prediction of the metallic character of V_2C -based systems has been confirmed by recent electrical measurements on exfoliated V_2C MXene flakes [58]. In addition, several electronic properties, including mobilities and effective masses of the charge carriers, are presently under investigation in order to reach a better understanding of the electronic transport in such systems. These results are beyond the scope of the present work and will be published in another paper.

C. Vibrational analysis and Raman measurement

According to the crystal information of the V_2C and V_2CT_2 systems, the three atoms of the primitive cell in the V_2C monosheet give rise to six optical modes and three acoustic modes at the Γ point of the Brillouin zone. In V_2CF_2 , the five atoms of each primitive cell lead to 12 optical modes and three acoustic modes at the Γ point of the Brillouin zone. In $V_2C(OH)_2$, the seven atoms of each primitive cell lead to 18 optical modes and three acoustic modes at the Γ point of the Brillouin zone. The optical phonons in the center of the Brillouin zone can be classified with the following irreducible representations:

$$\Gamma_{\text{optical}}(V_2C) = \underbrace{E_g + A_{1g}}_{\text{Raman}} + \underbrace{A_{2u} + E_u}_{\text{IR}}, \quad (2)$$

$$\Gamma_{\text{optical}}(V_2CF_2) = \underbrace{2E_g + 2A_{1g}}_{\text{Raman}} + \underbrace{2A_{2u} + 2E_u}_{\text{IR}}, \quad (3)$$

$$\Gamma_{\text{optical}}(V_2C(OH)_2) = \underbrace{3E_g + 3A_{1g}}_{\text{Raman}} + \underbrace{3A_{2u} + 3E_u}_{\text{IR}}. \quad (4)$$

The vibrational frequencies of the symmetric structures of V_2C , V_2CF_2 , and $V_2C(OH)_2$ are listed in Table II. The correspondence between the vibrational modes of the three systems is determined according to the direction of the vibrations and the nature of the contributing atoms. Schematic representations of the Raman-active modes of the pristine V_2C are illustrated in Fig. 4.

TABLE II. Vibrational mode frequencies of the stable V_2C -based monosheets. E_g and E_u modes are doubly degenerate.

	Raman modes					
	E_g	A_{1g}	E_g	A_{1g}	E_g	A_{1g}
V_2C	224.4	358.9				
V_2CF_2	197.8	289.6	281.6	525.6		
$V_2C(OH)_2$	214.3	301.1	296.6	530.2	443.2	3613.3
	IR modes					
	A_{2u}	E_u	E_u	A_{2u}	E_u	A_{2u}
V_2C	610.4	700.8				
V_2CF_2	636.0	761.0	221.3	442.8		
$V_2C(OH)_2$	627.4	757.5	285.5	446.7	435.7	3600.0

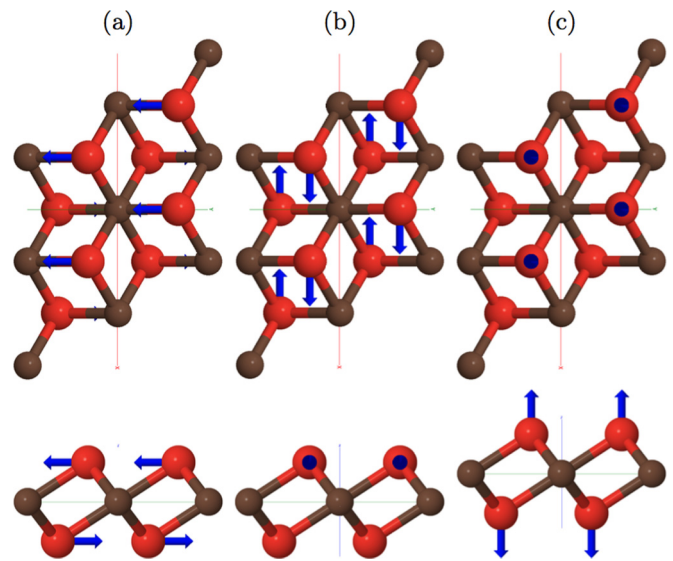


FIG. 4. Schematic representations of the Raman-active modes of pristine V_2C MXene: (a) and (b) in-plane vibration of V atoms at 224.4 cm^{-1} corresponding to the E_g mode and (c) out-of-plane vibration of V atoms at 358.9 cm^{-1} corresponding to the A_{1g} mode. Vanadium atoms are in red (light gray) and carbon atoms are in brown (dark gray).

Knowledge of the phonon spectrum of a material is essential for understanding a wide set of macroscopic properties, including the electrical and thermal conductivities. The phonon spectrum of V_2C was recently reported by Gao *et al.* [42], highlighting the stability of the system. Phonon dispersions and phonon densities of states (PhDOSs) for the V_2C , V_2CF_2 , and $V_2C(OH)_2$ monosheets are presented in Figs. 5(a)–5(c). These phonon band structures are plotted along the path $\Gamma(0,0,0) \rightarrow M(1/2,0,0) \rightarrow K(1/3,1/3,0) \rightarrow \Gamma(0,0,0)$. The phonon dispersions have three acoustic modes. Two of them exhibit a linear dispersion near Γ and correspond to in-plane rigid-body motions. In contrast, the third acoustic mode corresponding to out-of-plane vibration has a quadratic dispersion close to Γ and a lower energy in the rest of the spectrum. This quadratic dependence is analogous to the one observed in graphene [59] and in MoS_2 [60]. In Fig. 5(a), the vibrations of the V_2C system are below 750 cm^{-1} . The highest peaks in energy in the PhDOS corresponding to the vibration of carbon atoms have a large intensity due to the flatness of the bands around Γ . Moreover, the first three optical branches in the phonon spectrum demonstrate significantly lower frequencies close to the three acoustic phonon branches, thus inducing a phonon gap of about 250 cm^{-1} between the lower three and the upper three optical branches. This is a general property of MXenes and has already been observed previously in several MXene systems [14]. For the functionalized forms, this phonon gap between optical phonons is filled by additional optical phonon branches. This makes the most noticeable difference between pristine and terminated MXene systems. The phonon spectra of the terminated V_2CT_2 systems [Figs. 5(b) and 5(c)] reveal that the highest optical phonon frequencies are between 750 and 800 cm^{-1} , slightly larger than for the pristine case.

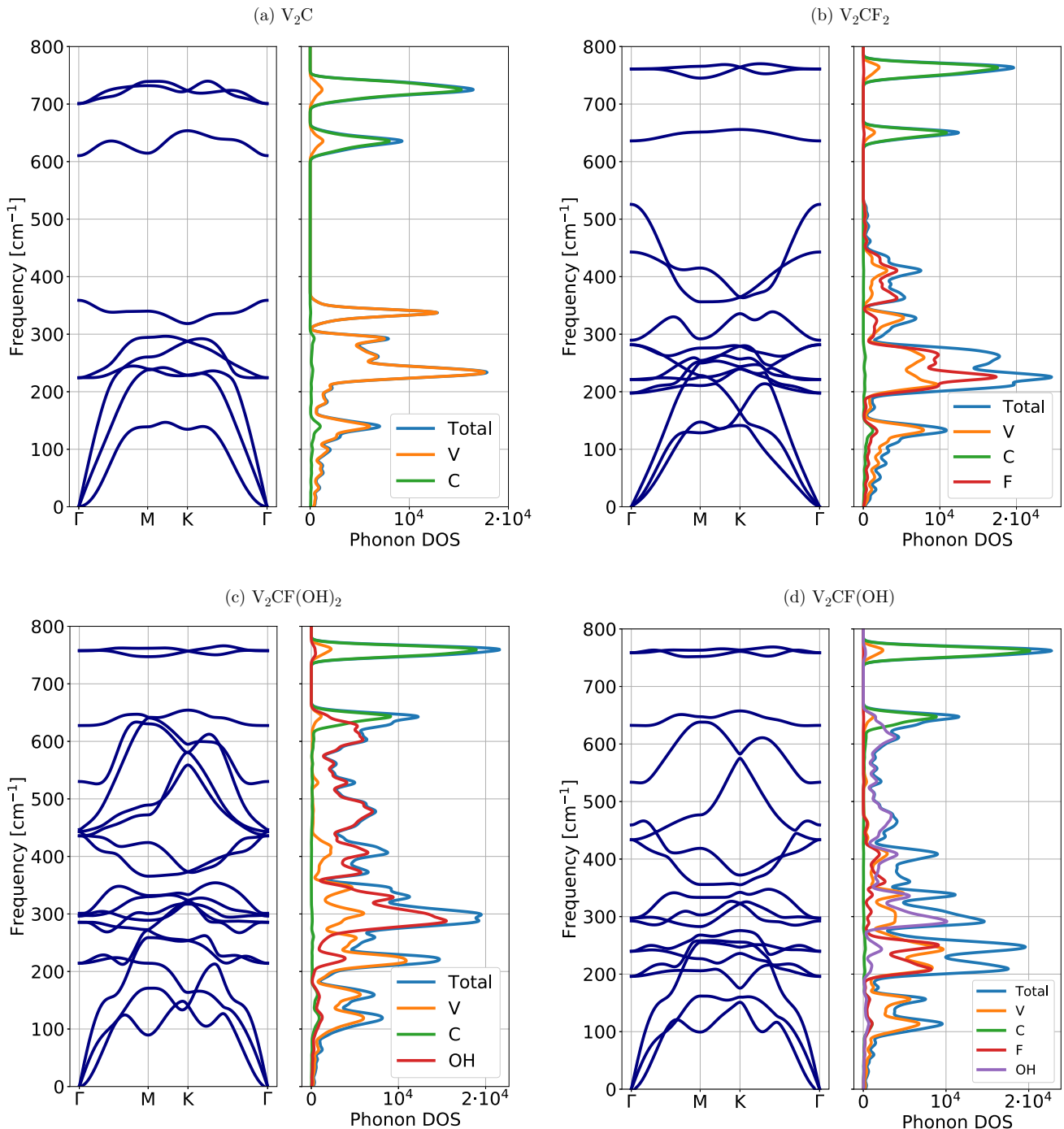


FIG. 5. Phonon band structures and densities of states of (a) V_2C , (b) V_2CF_2 , (c) $V_2C(OH)_2$, and (d) $V_2CF(OH)$ in their high-symmetry nonmagnetic configuration. For the three systems, the phonon density of states for each atom is also plotted, allowing for better visualization of the contributing atoms in each normal mode.

To further understand the role played by the surface functionalization in the MXene layer and its influence on the vibrational properties, the Raman- and infrared- (IR) active frequencies of the three monosheets are compared.

First of all, as presented in Table II, all terminal atoms strongly influence the normal-mode frequencies calculated for pristine V_2C . Regarding the Raman-active frequencies, the doubly degenerate E_g modes at 224 cm^{-1} and the A_{1g} mode at 359 cm^{-1} in the pristine V_2C monosheet correspond to in-

plane vibration [Figs. 4(a) and 4(b)] and out-of-plane vibration of V atoms [Fig. 4(c)], respectively. The E_g frequency shifts to lower wave numbers upon terminating with F and OH functional groups. The A_{1g} mode is softened to 290 and 301 cm^{-1} upon functionalization with $-F$ and $-OH$ groups. Since their main contributions are from vibrations of V atoms, it can be inferred that the vibrations of the terminal atoms weaken the motion of the V atoms. The IR-active frequencies located at 610 and 701 cm^{-1} correspond to out-of-plane

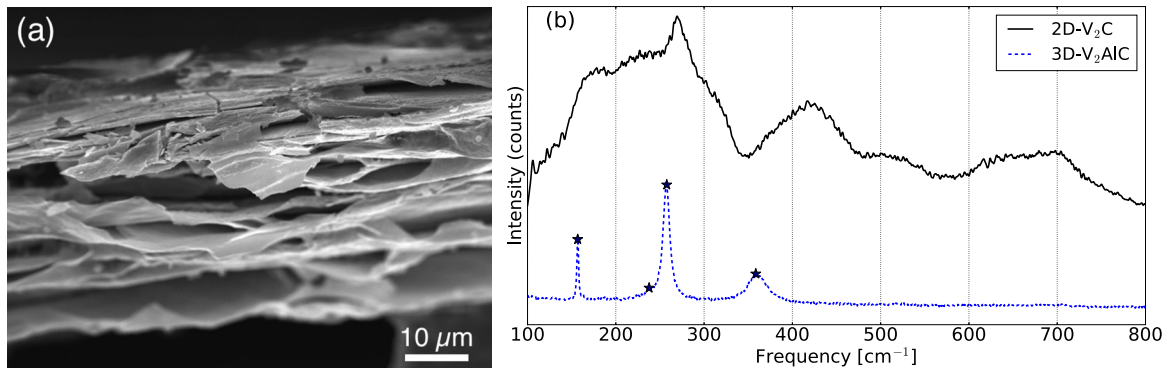


FIG. 6. (a) Scanning electron microscopy image and (b) Raman spectrum of the 3D MAX V_2AIC and the 2D MXene produced by HF etching of a V_2AIC sample. Note the sample consists of the stacking of numerous 2D layers, with curved paperlike morphology.

of C atoms (A_{2u} mode) and in-plane motion of C atoms (doubly degenerated E_u modes), respectively. The former mode at 610 cm^{-1} shifts to 636 and 627 cm^{-1} , while the latter one at 701 cm^{-1} is shifted to 761 and 758 cm^{-1} when terminating with F and OH groups, respectively. Therefore, the functional groups tend to strengthen both in-plane and out-of-plane motions of C atoms.

The remaining modes are attributed to the in-plane and out-of-plane vibrations of $-F$ and $-OH$ groups. The phonon mode at about 3600 cm^{-1} in the $V_2C(OH)_2$ monosheet is dominated by the vibration of the $-OH$ terminal groups. In the V_2CF_2 monosheet, the frequencies around 500 cm^{-1} are due to collaborative vibrations of V and F atoms. Collaborative vibrations of V and OH are also observed around 500 cm^{-1} in $V_2C(OH)_2$. As the terminal $-F$ and $-OH$ groups strongly

bond with V, the band gap centered around 500 cm^{-1} in the V_2C monosheet disappears in V_2CT_2 ($T = F, OH$). Lower-frequency phonons are due to collaborative motion of all atoms in the monosheets [Figs. 5(a)–5(c)].

Thanks to its sensitivity to very small changes in crystal structures, Raman spectroscopy is used to characterize the composition and quality of samples. However, before it can be used for this purpose, it is fundamental to properly define the peak positions and to assign them to the phonons computed at the Brillouin zone center (Γ point). This allows us to identify the contribution of each atom and group of atoms in the various vibrational modes corresponding to the reported peaks. The Raman spectrum of V_2C -based samples simply deposited on a glass slide is presented in Fig. 6(b). The comparison between the Raman spectrum of the 3D V_2AIC MAX phase

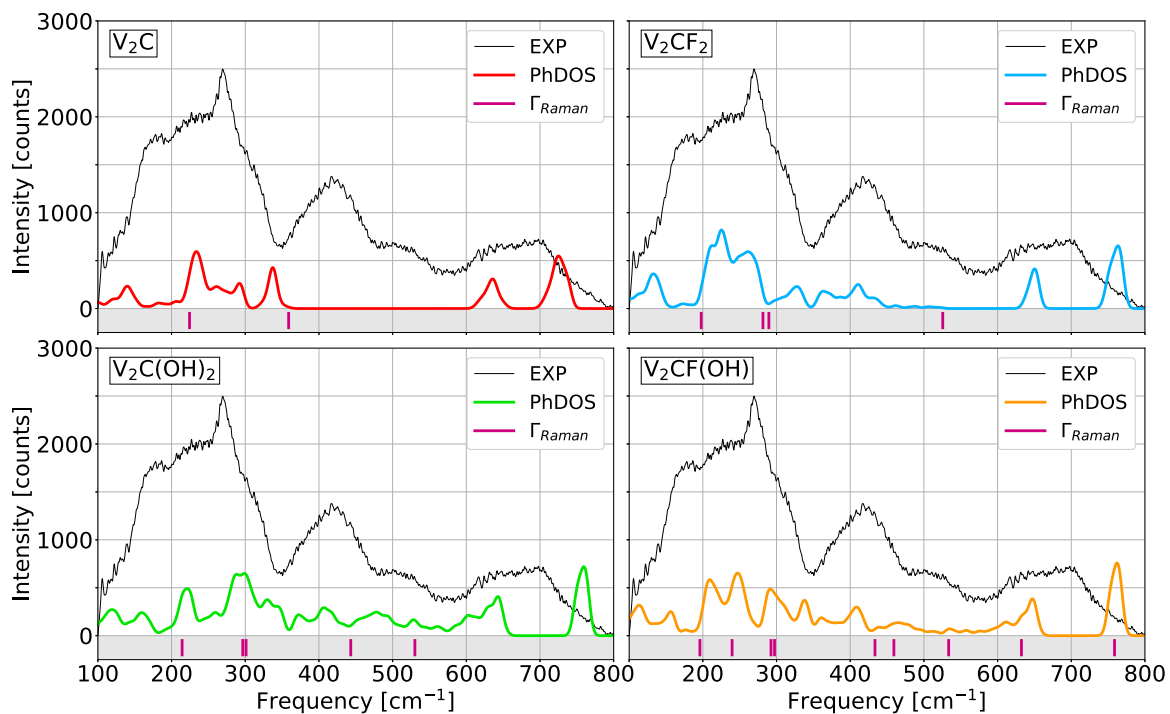


FIG. 7. Raman spectrum of the exfoliated V_2C -based sample collected at room temperature. The calculated Raman-active frequencies and the total phonon densities of states of the V_2C , V_2CF_2 , $V_2C(OH)_2$, and $V_2CF(OH)$ monosheets are also included under the experimental spectrum for comparison. The matching between the predicted normal-mode frequencies and the experimental spectrum confirms the presence of heterogeneous terminal groups randomly distributed at the V_2C surface.

TABLE III. Raman- and IR-active vibrational modes of stable V_2C -based systems with heterogeneous functional groups. All the vibrational modes are Raman and IR active.

	MD	E	E	A_1	E	E	A_1	A_1	A_1	E	A_1
V_2CFO	MD2	188.1	214.7	290.7	394.7	497.5	584.3		704.0	723.0	
$V_2CF(OH)$	MD2	196.0	239.7	292.5	297.3	433.6	459.3	533.6	632.4	758.7	3616.6
$V_2CO(OH)$	MD2	202.9	227.4	293.7	342.7	381.9	531.1	573.5	696.6	696.7	3652.6

and the corresponding 2D V_2C MXene system indicates a global reduction of the peak intensities and a broadening of the peaks, probably due to the larger interlayer spacing in the 2D system with respect to its 3D counterpart. Globally speaking, the two Raman spectra are very different, with sharp and well-defined peaks in the Raman spectrum of V_2AlC in contrast to those observed in the Raman spectrum of V_2C . Four peaks are identified in the V_2AlC spectrum at 158 cm^{-1} (E_{2g}), 239 cm^{-1} (E_{2g}), 258 cm^{-1} (E_{1g}), and 360 cm^{-1} (A_{1g}) [61]. The first two peaks, corresponding to in-plane vibrations of V and Al atoms, seem to completely disappear due to the removal of Al atoms, as confirmed by our EDS measurements [54]. The other two peaks, corresponding, respectively, to in-plane and out-of-plane vibrations of V atoms, can still find an equivalent in the V_2C spectrum, as confirmed by our theoretical prediction of an E_g mode around 224 cm^{-1} and an A_{1g} mode around 359 cm^{-1} for the V_2C system. In addition, as the etching process involves the substitution of Al atoms with lighter elements (F, OH), additional peaks can be observed at higher frequencies. These features make us confident in the achievement of the etching process and the resulting removal of the Al atoms from the V_2AlC sample. The calculated Raman-active frequencies of both V_2C and V_2CT_2 systems are reported in Table II and also illustrated in Fig. 7. The predicted peak positions for the V_2C monolayer are not sufficient to describe the experimental Raman spectrum, especially above 400 cm^{-1} . Upon termination with $-F$ and $-OH$ groups, additional Raman frequencies appear around 525 cm^{-1} and around $443, 530, \text{ and } 3613\text{ cm}^{-1}$, respectively. These frequencies roughly match most of the bands in the collected spectrum, and it turns out that the peaks around 430 and 530 cm^{-1} are clearly indicative of terminated V_2CT_2 MXene. The peak around 3600 cm^{-1} in the experimental spectrum confirms the presence of $-OH$ terminal groups at the sample surface. However, there are still some discrepancies between the theoretical predictions and the experimental Raman frequencies, as some predicted frequencies do not correspond to any Raman bands and vice versa. More specifically, the theoretical simulations of both pristine and terminated V_2C MXenes are not able to describe the hump between 600 and 700 cm^{-1} . Different factors can explain these deviations. First, the calculations are performed for homogeneous terminal groups, while the surface of our exfoliated sample is randomly terminated with both $-F$ and $-OH$ groups [22]. Second, the calculations deal with flat monolayers, while our sample consists of a stacking of sheets including stress and corrugations [Fig. 6(a)]. For instance, the presence of intrinsic defects such as vacancies and adatoms was evident in $Ti_3C_2T_x$ systems [37].

With the hope to improve the agreement between the experiment and the theoretical predictions, we investigate the effect of heterogeneous termination of the Raman-active

modes. Using the same principles as for the homogeneous functionalization, the $V_2CF(OH)$ monosheet (F terminated on one side and OH terminated on the other side of the monosheet) is built. The four models (MD1–MD4) are tested, and it is found that an equivalent of MD2 is the most energetically favorable configuration (Table I). As presented in Fig. 2(d), $V_2CF(OH)$ is still electrically conductive. The heterogeneity of the terminal groups induces a difference in the V-T bonding lengths on both sides of the MXene layer. As the reduced coordinates are modified, the Wyckoff positions are influenced, and hence, the space group is moved to $P3m1$ (156). For such a configuration, the irreducible representation is given by

$$\Gamma_{\text{optical}}(V_2CF(OH)) = \underbrace{5A_1 + 5E}_{\text{Raman+IR}} \quad (5)$$

for $V_2CF(OH)$. The normal-mode frequencies for this system are listed in Table III and compared to the experimentally collected Raman spectrum in Fig. 7(d).

There are four main additional Raman-active modes at $434, 459, 632, \text{ and } 759\text{ cm}^{-1}$ with respect to the homogeneous situations. The first two peaks match well with the band around 430 cm^{-1} , and the last two peaks match well with the hump centered at 650 cm^{-1} in the experimental spectrum. This close matching between the theoretically predicted positions of the Raman-active peaks and the experimental Raman spectrum reflects the fact that the terminal groups are actually heterogeneous and most likely randomly distributed at the V_2C surface.

Table IV summarizes the assignment of the experimental peaks to the theoretical predictions. These results suggest that the presence of Raman peaks between 400 and 550 cm^{-1} is indicative of terminated V_2CT_2 systems, while the peak centered at 650 cm^{-1} seems to originate from the presence of heterogeneous functional groups at the sample surface. The presence of $-OH$ groups gives rise to a peak around 3600 cm^{-1} in the experimental spectrum. The deviations between the computed and collected Raman frequencies are reported in Table IV and indicate that the experimental Raman frequencies are correctly predicted, with maximal deviations of 15% and 3% in the low- and high-frequency ranges, respectively.

IV. CONCLUSIONS

In conclusion, the static and dynamical properties of pristine bare V_2C and terminated V_2CT_2 ($T = F, O, \text{ and } OH$) monosheets have been investigated using first-principles techniques. This work gives insight into the structural, electronic, and vibrational properties of an emerging 2D material. The optimized crystal structure of V_2C is dynamically stable. It is also found that the surface functionalization with F and OH groups is energetically favorable, in contrast to oxygen termination. Regarding the electronic properties, both V_2C

TABLE IV. Experimental Raman peak positions compared to the predicted Raman-active frequencies computed for V_2C , V_2CF_2 , $V_2C(OH)_2$, and $V_2CF(OH)$ monosheets. The last row corresponds to the maximal deviation of the computed frequencies for $V_2CF(OH)$ with respect to the experimental data.

Expt. spectrum	Raman frequencies (cm^{-1})						
	~ 170	~ 230	~ 270	~ 430	~ 540	~ 650	~ 3600
V_2C		224	359				
V_2CF_2		198	282, 290		526		
$V_2C(OH)_2$		214	297, 301	443	530		3613
$V_2CF(OH)$	196	240	293, 297	434, 459	534	632	3617
$\Delta_{\text{MAX}}(\%)$	15	4	10	7	1	3	0.5

and V_2CT_2 ($T = \text{F, OH}$) systems are metallic. The electronic bands crossing the Fermi level come from V $3d$ orbitals. The analysis of the phonon dispersion and PDOS of the bare V_2C monosheet demonstrates the presence of a phonon gap between the three lowest and the three highest optical branches. Upon functionalization, such a phonon band gap disappears as the gap is bridged by vibrations of the terminal groups (F and OH). It was shown that the terminal atoms weaken the motions in which the V atoms are involved while strengthening the vibrations of the C atoms. The corresponding vibrational frequencies are drastically changed when the nature of the functional group is modified. Vibrational properties were computed with the aim to understand and characterize the origin of the Raman-active peaks in the experimental spectrum. A first attempt to assign the atomic motions to the experimental Raman peaks was proposed. The comparison of our theoretical predictions with the experimental Raman spectrum gives a satisfying agreement, as both the number of peaks and their positions are well described, especially when considering mixed terminal groups at the MXene's surface. The list of central peak frequencies for each hump in the experimental spectrum reported in Table IV can thus be considered a signature of V_2C samples with different chemical terminations.

This work is a prerequisite to experimental nondestructive identification and synthesis of V_2C -based 2D materials.

ACKNOWLEDGMENTS

This work was supported by the UCL through a FSR Grant (A.C.) and by the FRS-FNRS through a FRIA Grant (L.S.). The authors acknowledge financial support from the Fédération Wallonie-Bruxelles through the Action de Recherche Concertée (ARC) on 3D nanoarchitecturing of 2D crystals (Project No. 16/21-077), from the European Union's Horizon 2020 researchers and innovation program (Project No. 696656), and from the Belgium FNRS. The authors are also indebted to the Flag-ERA JTC 2017 project entitled "MORE-MXenes." Computational resources were provided by the supercomputing facilities of the Université catholique de Louvain (CISM/UCL) and the Consortium des Equipements de Calcul Intensif en Fédération Wallonie Bruxelles (CECI) funded by the Fonds de la Recherche Scientifique de Belgique (F.R.S.-FNRS) under Convention No. 2.5020.11. Crystal growth was financially supported by the Agence Nationale de la Recherche through Project No. ANR-13-BS09-0024. All structural models were rendered using VESTA [62] and JMOL [63].

- [1] K. S. Novoselov, A. K. Geim, S. V. Morozov, D. Jiang, Y. Zhang, S. V. Dubonos, I. V. Grigorieva, and A. A. Firsov, *Science* **306**, 666 (2004).
- [2] K. S. Novoselov, D. Jiang, F. Schedin, T. J. Booth, V. V. Khotkevich, S. V. Morozov, and A. K. Geim, *Proc. Natl. Acad. Sci. U.S.A.* **102**, 10451 (2005).
- [3] A. K. Geim and I. V. Grigorieva, *Nature (London)* **499**, 419 (2013).
- [4] L. Song, *Nano Lett.* **10**, 3209 (2010).
- [5] Q. H. Wang, K. Kalantar-Zadeh, A. Kis, J. N. Coleman, and M. S. Strano, *Nat. Nanotechnol.* **7**, 699 (2012).
- [6] B. Lalmi, H. Oughaddou, H. Enriquez, A. Kara, S. Vizzini, B. Ealet, and B. Aufray, *Appl. Phys. Lett.* **97**, 223109 (2010).
- [7] H. Liu, A. T. Neal, Z. Zhu, Z. Luo, X. Xu, D. Tomanek, and P. D. Ye, *Nano* **8**, 4033 (2014).
- [8] S. Cahangirov, M. Topsakal, E. Akturk, H. Sahin, and S. Ciraci, *Phys. Rev. Lett.* **102**, 236804 (2009).
- [9] M. Davila, L. Xian, S. Cahangirov, A. Rubio, and G. L. Lay, *New J. Phys.* **16**, 095002 (2014).
- [10] M. Naguib, M. Kurtoglu, V. Presser, J. Lu, J. Niu, M. Heon, M. Hultman, Y. Gogotsi, and M. W. Barsoum, *Adv. Mater.* **23**, 4248 (2011).
- [11] M. Naguib, O. Mashtalir, J. Carle, V. Presser, J. Lu, L. Hultman, Y. Gogotsi, and M. W. Barsoum, *ACS Nano* **6**, 1322 (2012).
- [12] M. Naguib, V. N. Mochalin, M. W. Barsoum, and Y. Gogotsi, *Adv. Mater.* **26**, 992 (2014).
- [13] B. Anasori, Y. Xie, M. Beidaghi, J. Lu, B. C. Hosler, L. Hultman, P. R. C. Kent, Y. Gogotsi, and M. W. Barsoum, *ACS Nano* **9**, 9507 (2015).
- [14] U. Yorulmaz, A. Ozden, N. K. Perkgoz, F. Ay, and C. Sevik, *Nanotechnology* **27**, 335702 (2016).
- [15] M. R. Lukatskaya, B. Dunn, and Y. Gogotsi, *Nat. Commun.* **7**, 12647 (2016).
- [16] Q. Hu, D. Sun, Q. Wu, H. Wang, L. Wang, B. Liu, A. Zhou, and J. He, *J. Phys. Chem. A* **117**, 14253 (2013).
- [17] O. Mashtalir, M. Naguib, V. N. Mochalin, Y. Dall'Agnesse, M. Heon, M. W. Barsoum, and Y. Gogotsi, *Nat. Commun.* **4**, 1716 (2013).

- [18] M. Naguib, J. Halim, J. Lu, K. M. Cook, L. Hultman, Y. Gogotsi, and M. W. Barsoum, *J. Am. Chem. Soc.* **135**, 15966 (2013).
- [19] Q. Tang, Z. Zhou, and P. Shen, *J. Am. Chem. Soc.* **134**, 16909 (2012).
- [20] J. Hu, B. Xu, C. Ouyang, S. A. Yang, and Y. Yao, *J. Phys. Chem. C* **118**, 24274 (2014).
- [21] M. Ghidui, M. R. Lukatskaya, M. Q. Zhao, Y. Gogotsi, and M. W. Barsoum, *Nature (London)* **516**, 78 (2014).
- [22] K. J. Harris, M. Bugnet, M. Naguib, M. W. Barsoum, and G. R. Goward, *J. Phys. Chem. C* **119**, 13713 (2015).
- [23] M. R. Lukatskaya, O. Mashtalir, C. E. Ren, Y. Dall'Agnese, P. Rozier, P. L. Taberna, M. Naguib, P. Simon, M. W. Barsoum, and Y. Gogotsi, *Science* **341**, 1502 (2013).
- [24] Y. Dall'Agnese, M. R. Lukatskaya, K. M. Cook, P.-L. Taberna, Y. Gogotsi, and P. Simon, *Electrochem. Commun.* **48**, 118 (2014).
- [25] R. B. Rahki, B. Ahmed, M. N. Hedhili, D. H. Anjum, and H. N. Alshareef, *Chem. Mater.* **27**, 5314 (2015).
- [26] Y. Dall'Agnese, P.-L. Taberna, Y. Gogotsi, and P. Simon, *J. Phys. Chem. Lett.* **6**, 2305 (2015).
- [27] X. Ji, K. Xu, C. Chen, B. Zhang, H. Wan, Y. Ruan, L. Miao, and J. Jiang, *J. Mater. Chem. A* **3**, 9909 (2015).
- [28] M. Khazaei, M. Arai, T. Sasaki, C. Y. Chung, N. S. Venkataraman, M. Estili, Y. Sakka, and Y. Kawazoe, *Adv. Funct. Mater.* **23**, 2185 (2013).
- [29] X. F. Yu, Y. C. Li, J. B. Cheng, Z. B. Liu, Q. Z. Li, W. Z. Li, X. Yanh, and B. Xiao, *ACS Appl. Mater. Interfaces* **7**, 13707 (2015).
- [30] H. Liu, C. Duan, C. Yang, W. Shen, F. Wang, and Z. Zhu, *Sens. Actuators B* **218**, 60 (2015).
- [31] J. Come, J. M. Black, M. R. Lukatskaya, M. Naguib, M. Beidaghi, A. J. Rondinone, S. V. Kalinin, D. J. Wesolowski, Y. Gogotsi, and N. Balke, *Nano Energy* **17**, 27 (2015).
- [32] M. Kurtoglu, M. Naguib, Y. Gogotsi, and M. W. Barsoum, *MRS Commun.* **2**, 133 (2012).
- [33] Z. Guo, J. Zhou, C. Si, and Z. Sun, *Phys. Chem. Chem. Phys.* **17**, 15348 (2015).
- [34] S. Zhao, W. Kang, and J. Xue, *Appl. Phys. Lett.* **104**, 133106 (2014).
- [35] C. Si, J. Zhou, and Z. Sun, *ACS Appl. Mater. Interfaces* **7**, 17510 (2015).
- [36] M. W. Barsoum, *Prog. Solid State Chem.* **28**, 201 (2000).
- [37] L. H. Karlsson, J. Birch, J. Halim, M. W. Barsoum, and P. O. Persson, *Nano Lett.* **15**, 4955 (2015).
- [38] H. W. Wang, M. Naguib, K. Page, D. J. Wesolowski, and Y. Gogotsi, *Chem. Mater.* **28**, 349 (2016).
- [39] J. Halim, K. C. Cook, M. Naguib, P. Eklund, Y. Gogotsi, J. Rosen, and M. W. Barsoum, *Appl. Surf. Sci.* **362**, 406 (2016).
- [40] P. Hohenberg and W. Kohn, *Phys. Rev.* **136**, B864 (1964).
- [41] W. Kohn and L. J. Sham, *Phys. Rev.* **140**, A1133 (1965).
- [42] G. Gao, G. Ding, J. Li, K. Yao, M. Wu, and M. Qian, *Nanoscale* **8**, 8986 (2016).
- [43] S. Baroni, P. Giannozzi, and A. Testa, *Phys. Rev. Lett.* **58**, 1861 (1987).
- [44] X. Gonze, *Phys. Rev. A* **52**, 1086 (1995).
- [45] T. Hu, J. Wang, H. Zhang, Z. Li, M. Hu, and X. Wang, *Phys. Chem. Chem. Phys.* **17**, 9997 (2015).
- [46] X. Gonze, G.-M. Rignanese, M. Verstraete, J.-M. Beuken, Y. Pouillon, R. Caracas, F. Jollet, M. Torrent, G. Zerah, M. Mikami, P. Ghosez, M. Veithen, J.-Y. Raty, V. Olevano, F. Bruneval, L. Reining, R. Godby, G. Onida, D. R. Hamann, and D. C. Allan, *Zeitschrift für Kristallographie* **220**, 558 (2005).
- [47] X. Gonze, B. Amadon, P.-M. Anglade, J.-M. Beuken, F. Bottin, P. Boulanger, F. Bruneval, D. Caliste, R. Caracas, M. Coté, T. Deutsch, L. Genovese, P. Ghosez, M. Giantomassi, S. Goedecker, D. R. Hamann, P. Hermet, F. Jollet, G. Jomard, S. Leroux, M. Mancini, S. Mazevet, M. J. T. Oliveira, G. Onida, Y. Pouillon, T. Rangel, G.-M. Rignanese, D. Sangalli, R. Shaltaf, M. Torrent, M. J. Verstraete, G. Zerah, and J. W. Zwanziger, *Comput. Phys. Commun.* **180**, 2582 (2009).
- [48] J. P. Perdew, K. Burke, and M. Ernzerhof, *Phys. Rev. Lett.* **77**, 3865 (1996).
- [49] V. I. Anisimov, I. V. Solovyev, M. A. Korotin, M. T. Czyżyk, and G. A. Sawatzky, *Phys. Rev. B* **48**, 16929 (1993).
- [50] V. I. Anisimov, F. Aryasetiawan, and A. I. Lichtenstein, *J. Phys. Condens. Matter* **9**, 767 (1997).
- [51] D. O. Scanlon, A. Walsh, B. J. Morgan, and G. W. Watson, *J. Phys. Chem. C* **112**, 9903 (2008).
- [52] D. R. Hamann, *Phys. Rev. B* **88**, 085117 (2013).
- [53] L. Shi, T. Ouisse, E. Sarigiannidou, O. Chaix-Pluchery, H. Roussel, D. Chaussende, and B. Hackens, *Acta Mater.* **83**, 304 (2015).
- [54] L. Shi, T. Ouisse, and B. Hackens (unpublished).
- [55] M. Ashton, K. Mathew, R. G. Hennig, and S. B. Sinnott, *J. Phys. Chem. C* **120**, 3550 (2016).
- [56] M. Khazaei, A. Ranjbar, M. Ghorbani-Asl, M. Arai, T. Sasaki, Y. Liang, and S. Yunoki, *Phys. Rev. B* **93**, 205125 (2016).
- [57] J. M. Schneider, R. Mertens, and D. Music, *J. Appl. Phys.* **99**, 013501 (2006).
- [58] L. Shi, A. Champagne, T. Ouisse, B. Hackens, and J.-C. Charlier (unpublished).
- [59] M. S. Dresselhaus and P. C. Eklund, *Adv. Phys.* **49**, 705 (2000).
- [60] A. Molina-Sanchez and L. Wirtz, *Phys. Rev. B* **84**, 155413 (2011).
- [61] J. E. Spanier, S. Gupta, M. Amer, and M. W. Barsoum, *Phys. Rev. B* **71**, 012103 (2005).
- [62] K. Momma and F. Izumi, *J. Appl. Crystallogr.* **41**, 653 (2008).
- [63] A. Herraez, *Biochem. Mol. Biol. Educ.* **34**, 255 (2006).